RED SUPERGIANT NUCLEOSYNTHESIS AND MIXING IN THE MAGELLANIC CLOUDS

Caroline McCormick
Department of Astronomy, University of Virginia

Advisors: Dr. Steven R. Majewski and Dr. Verne V. Smith
April 22, 2025

Abstract

Understanding how stars evolve is of great importance because they produce most of the heavy elements ("metals") in the universe today. We seek to test theoretical understanding of how internal stellar mixing during the red supergiant (RSG) phase of evolution is affected by stellar mass and metallicity. We first isolated 2,091 RSGs from the APOGEE survey located in two nearby galaxies–the Large and Small Magellanic Clouds. We then estimated bolometric luminosities and stellar masses to better characterize our sample stars. Finally, we derived C, N, O, and ^{12}C/^{13}C abundances for the RSGs using the BACCHUS spectral analysis code and observed spectra. Our initial results provide evidence through low $\log(C/N)$ and ^{12}C/^{13}C ratios that rotational and/or convective mixing has occurred in our RSGs. We also observe that mixing is more efficient as metallicity decreases, since the SMC exhibits a larger change in $\log(C/N)$ compared to the LMC. Further analysis is needed to conclusively say how mixing changes with mass, and to test if all aspects of stellar evolution theory hold for low-metallicity RSGs. Future efforts will include deriving more accurate stellar masses to probe how these ratios change with mass and finding quantitatively appropriate models for the Magellanic Clouds.

Introduction

Stars are critical to understand because they are the driving force behind the chemical evolution of galaxies and the universe as a whole. Starting with gas made up of mostly H and He, stars undergo several phases of nucleosynthesis (i.e., the creation of nucleii) deep within their interiors to fuse light atoms into progressively heavier atoms. In particular, massive stars[1] will successively "burn" through H, He, C, Ne, O, and Si in the stellar core and in thin shells outside the core. These nuclear burning episodes produce many metals[2] including the next burning phase's seed material and intermediate burning products, such as ^{14}N and ^{13}C in the case of H burning. Eventually, the material left at the end of a massive star's life returns to the interstellar medium (ISM) when the star explodes and dies.

Nuclear burning depends on several conditions including temperature, density of the gas, and the amount of source material available. For most of a massive star's life, it will fuse H into He in the core of the star through a process called the CNO cycle. The CNO cycle uses C, N, and O as catalysts to generate He from H. If a star begins life with a sig-

[1] We define massive stars to be stars with initial mass $\gtrsim 8M_{\odot}$.

[2] Astronomers refer to any element heavier than He as a metal.

nificant rotation rate, this rotation can cause the material in the core to diffuse outward, moving some of the source material and intermediate burning products to layers of the star where nuclear burning cannot take place (e.g., Georgy et al. 2013b).

Once the star has used all of its H supply in the core, the star evolves to the red supergiant (RSG) phase of evolution where it moves first to shell-H burning, then to additional shell and core burning phases with successively heavier elements used as source material.[3] At the beginning of the RSG phase, the outer layers of the star form deep convective zones. These convective zones reach into regions of the star that contain partially processed material from previous burning episodes. Over time, these convective zones deepen to dredge up more material to the surface of the star (e.g., Davies & Dessart 2019).

Observationally, we see a decrease in the C/N and ^{12}C/^{13}C ratios when the star becomes a RSG, which can be the combined effect of rotational mixing that occurs during core-H burning and deep convective mixing during the RSG phase. Primarily ^{14}N and ^{13}C are dredged up to the surface of the star by the convective envelope from the burning region where they were produced at the expense of ^{12}C. Current stellar evolution theory dictates that more massive RSGs have a larger relative amount of ^{14}N and ^{13}C compared to ^{12}C than less massive RSGs at the end of their lives (Davies & Dessart 2019). The reasoning behind this statement is that more massive stars have larger cores at birth, so more material is available to partake in core nuclear burning. Therefore, more partially burned material can be dredged up by the convective envelope over the star's life.

Rotational mixing and convective mixing play critical roles in the evolution of the star as they alter the material available to the star in nuclear burning regions, which affect the phases the star evolves through and how long the star can live. Therefore, understanding how these mixing processes are correlated with stellar parameters like mass and metallicity are crucial for understanding the larger picture of what material is ultimately returned to the ISM to be used in galaxies.

In this work, we aim to add a large, homogeneously derived sample of CNO abundance observations to the literature. It is our hope that these observations will provide insight into how rotational and convective mixing vary based on stellar parameters such as mass and metallicity during the RSG phase of evolution. We seek to compare our observational abundances to theoretical predictions to test our understanding of stellar evolution and provide constraints for these mixing processes and nucleosynthesis in future modeling efforts.

To accomplish these goals, we estimate CNO abundances for approximately 2,000 low-metallicity RSGs in the Large and Small Magellanic Clouds (LMC and SMC), two satellite galaxies of the Milky Way. Studying RSGs in these environments gives us an opportunity to test if our understanding of massive star evolution applies to stars in galaxies other than our own on a large scale.

The data used in this project are described below, along with an explanation of how we estimated relevant stellar parameters for our RSGs. We then discuss how the CNO abundances were estimated from the RSG stellar spectra. Finally, we show our current results while discussing areas of promise, concern, and next steps in this ongoing project.

Data

This work utilizes data from the Sloan Digital Sky Survey IV's (SDSS-IV; Blanton et al. 2017) Apache Point Observatory Galactic Evolution Experiment (APOGEE; Majewski et al. 2017). Specifically, stellar parameters and H-band spectra were adopted from the 17th Data Release (DR17; Abdurro'uf et al. 2022) of the APOGEE survey, which includes observations of cool stars in the Magellanic

[3] A massive star can have multiple RSG phases where there are different nuclear burning processes occurring at various locations within the star.

Clouds (MCs) made by the APOGEE-S spectrograph (Wilson et al. 2019) on the 2.5-meter du Pont Telescope (Bowen & Vaughan, 1973) at Las Campanas Observatory in Chile. The targeting for the MC stars and a description of the data reduction pipeline for the APOGEE-2 survey are described in Zasowski et al. (2017), Beaton et al. (2021), Santana et al. (2021), and Nidever et al. (2015).

The stellar parameters and abundances provided in APOGEE were derived using the APOGEE Stellar Atmospheric Parameters and Chemical Abundances Pipeline (ASPCAP; García Pérez et al. 2016). This pipeline was based on the FERRE code written by Allende Prieto et al. (2006). ASPCAP matches stellar atmospheric parameters to a grid of MARCS stellar atmospheres (Gustafsson et al., 2008; Jönsson et al., 2020) to derive chemical abundances for each star using the star's observed H-band spectrum, generated synthetic spectra, and an H-band line list describing the atomic and molecular spectral features found in the H band from Smith et al. (2021). For this project, we primarily utilize the following ASPCAP stellar parameters to characterize the evolutionary states of our sample stars: effective temperature (T_{eff}), surface gravity ($\log g$), and overall metallicity[4] ([M/H]).

Also included in the APOGEE DR17 catalog are near-infrared (J-, H-, and K_s-band) photometry for each star from the Two Micron All Sky Survey (2MASS; Skrutskie et al. 2006), which represent stellar brightnesses in specific wavelength ranges of light. Dust and gas present in the Milky Way and in the MCs can influence the observed brightness of a star. This material exists along the line of sight to a star, and it can absorb and scatter light (preferentially blue light) on its way to us. Therefore, the brightness of the stars that we observe in the MCs often appear dimmer and redder (i.e., longer wavelengths of light) than they would if we could observe their true brightnesses and colors without the influence of dust.

[4]"Metallicity" refers to the amount of elements heavier than He in a star.

Table 1: The spatial and kinematic parameters used to identify stars belonging to the MCs. Numbers in parentheses represent the range of acceptable values for each quantity.

Quantity	LMC	SMC
α_{center}	80.894°	13.187°
δ_{center}	-69.756°	-72.829°
D	12°	8°
RV [km/s]	(161, 370)	(66, 235)
μ_α [km/s]	(1.01, 2.62)	(0.05, 1.51)
μ_δ [km/s]	(-1.15, 1.70)	(-1.57, -0.94)

To correct for this observational artifact, we apply extinction correction factors to the brightnesses in each photometric band; these corrections characterize the total, wavelength-dependent amount of light missing due to the presence of dust. We assume the extinction law of Cardelli et al. (1989) to describe the relative amount of extinction in each photometric band. Using the K_s extinction corrections for each star from APOGEE, we calculated the extinction corrections in J and H bands (A_J and A_H) with the Cardelli Law:

$$\frac{A_J}{A_{Ks}} = 2.45 \quad \text{and} \quad \frac{A_H}{A_{Ks}} = 1.56 \qquad (1)$$

Red Supergiant Sample Selection

Because the APOGEE catalog includes a vast number of stars in the Milky Way and nearby galaxies, we first isolated all of the observed stars belonging to the MCs. The work of Hasselquist et al. (2021) outlines several selection criteria that separates APOGEE MC stars from other physical locations (summarized in Table 1). We first chose potential MC stars based on their physical location in the sky, which is specified by the right ascension (α) and declination (δ) parameters for each star. We selected all stars within a two-dimensional, projected distance (D) from the center of each Cloud (see Table 1 for the values) as likely belonging to the Cloud. To further ascertain if a star is a likely MC member,

Table 2: The CMD and luminosity cuts used to identify RSGs in the LMC and SMC.

LMC	
$8.5 < K_s \leq 12$:	$K_s \leq 25.46 - [13.542 \times (J - K_s)]$
$K_s \leq 8.5$:	$(J - K_s) \leq 1.8$
	$\log(L/L_\odot) > 3.66$
SMC	
$8.977 < K_s \leq 12.65$:	$K_s \leq (-13.333 \times [(J - K_s) + 0.034]) + 24.684$
$K_s \leq 8.977$:	$(J - K_s) \leq 1.75$
	$\log(L/L_\odot) > 3.66$

we limited the stars based on proper motions in right ascension (μ_α) and declination (μ_δ) measured by the Gaia satellite (early Data Release 3; Gaia Collaboration et al. 2021). Stars belonging to a specific galaxy exhibit similar proper motions to each other due to the collective motion of the galaxy, so we choose stars with proper motions $\pm 3\sigma$ from the median values for the LMC and SMC.

Finally, to account for the third spatial dimension (i.e., toward/away from the observer), we limited the sample based on the stars' radial velocities measured by APOGEE, which indicates how fast a star is moving away or toward an observer. To be characterized as a MC member, the star's radial velocity must fall within $\pm 3\sigma$ of the LMC or SMC median value. Like proper motion, MC stars will have radial velocities that differ from stars in other galaxies, helping us distinguish MC stars from foreground, Milky Way stars in our line of sight to the MCs.

Once our total MC sample was finalized, we chose only stars in the RSG phase of evolution. For the LMC, we followed the selection criteria from Neugent et al. (2020), who use the color-magnitude diagram (CMD) to define photometric cuts that separate the region RSGs occupy in the K_s vs $(J - K_s)$ CMD. Similarly for the SMC, we adopted CMD RSG cuts from Cioni et al. (2006a), Cioni et al. (2006b), and Boyer et al. (2011). Finally, to focus on high-mass RSGs (i.e., $M_{initial} \gtrsim 8 M_\odot$), we made a luminosity cut to require our stars to have $\log(L/L_\odot) > 3.66$. The CMD criteria used to obtain our MC RSG samples are shown in Table 2.

As a final check on our selected MC RSG stars, we required that the APOGEE data for these stars must be reasonable. Specifically, we exclude any star that has the "STAR BAD" flag set in the APOGEE catalog; this flag indicates that something about the observed data or a result from the ASPCAP pipeline is untrustworthy. We are left with 1,613 and 478 RSGs in the LMC and SMC, respectively, as seen in the Hertzsprung-Russell (HR) diagrams in Figure 1.

Derived Quantities

Bolometric Luminosity

Stellar parameters such as temperature, surface gravity, and metallicity aid in characterizing the phase of evolution a star is experiencing. A further critical stellar parameter to distinguish evolutionary phases is the bolometric luminosity. The bolometric luminosity describes the total brightness of a star across all wavelengths of light. It is an intrinsic property to the star that does not change based on the star's distance or environmental factors such as dust extinction. Furthermore, models that offer theoretical predictions of stellar evolution often make these predictions based on intrinsic properties of stars, so bolometric luminosity is necessary to compare observations to theory.

For the MC RSGs, we calculated bolometric luminosities with the following equation:

$$L = 10^{(M_{bol,\odot} - K_{s,0} - BC_{K_s} + \mu)/2.5} L_\odot \qquad (2)$$

L is in units of solar luminosities ($L_\odot$); $M_{bol,\odot}$

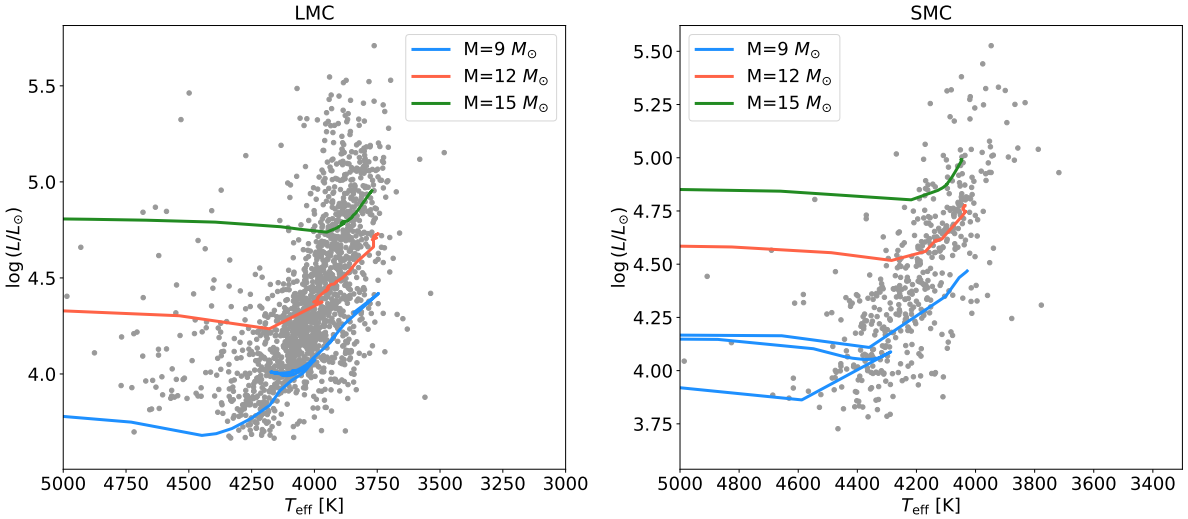

Figure 1: The HR diagram of the LMC and SMC RSGs in our sample. Overlaid are stellar evolutionary tracks from Georgy et al. (2013a) for typical RSG initial masses and for the average LMC and SMC metallicities of [M/H] = -0.38 and -0.86, respectively.

is the bolometric absolute magnitude of the Sun (4.74 $M_\odot$; Mamajek et al. 2015); $K_{s,0}$ is the extinction-corrected, apparent K_s magnitude; and BC_{K_s} is the K_s bolometric correction term. The bolometric correction terms are calculated from the ATLAS9 models (Kurucz 1993), and they are correction terms to estimate the amount of light that is emitted from a star across all wavelengths of light other than in the observed K_s band. Finally, μ is the distance modulus to each Cloud.

We assume a distance modulus of 18.477 $\pm$ 0.004 mag ($\backsim$49.6 kpc) for the LMC (Pietrzyński et al. 2019) and 18.977 $\pm$ 0.016 mag ($\backsim$62.4 kpc) for the SMC (Graczyk et al. 2020). These represent the average distances to the LMC and SMC, and for the purposes of this study, it is reasonable to assume that the internal distance variations for each Cloud from this average value negligibly affect our derived quantities.

Stellar Mass

The mass of a star is one of the most influential properties that affect the evolution of a star. The mass of a star dictates which phases of evolution it experiences, the length of time it goes through each phase, and what nucleosynthetic products are produced within the star to be returned to the ISM. From an observational perspective, we cannot measure the mass of a star directly, so we must utilize indirect methods to estimate the mass of a star.

The method used in this study relies on equations of stellar astrophysics. These equations relate stellar parameters deduced from spectroscopic observations (T_{eff} and $\log g$) and from photometry (L) to the mass of a star. Combining the following equations gives a relation with these quantities to estimate stellar mass (M):

$$L = 4\pi\sigma_{SB}R^2T_{eff}^4 \tag{3}$$

$$\log g = \log\left(\frac{GM}{R^2}\right) \tag{4}$$

$$M = \frac{10^{\log g}L}{4\pi\sigma_{SB}GT_{eff}^4} \tag{5}$$

In the aforementioned equations, σ_{SB} is the Stefan-Boltzmann constant; G is the gravitational constant; and R is the stellar radius. It is also important to emphasize that this technique is a rough estimation of the stellar mass, so the masses should be used a guide rather than absolute fact. There are many sources of potential error in this method, including uncertainty in measured quantities, errors in the modeling process that provides stellar param-

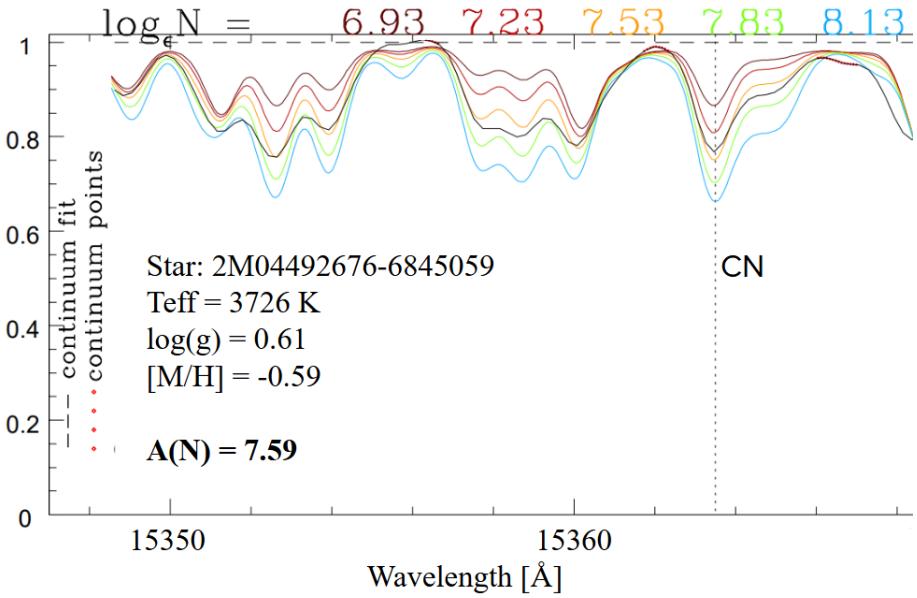

Figure 2: An example fit used to derive the N abundance from the 15363.5 $\AA$ CN spectral feature. The black curve is the observed spectrum, while the colored lines represent model spectra of the various N abundance values displayed at the top.

eter estimates, and/or poor distance assumptions that affect the luminosity calculation.

CNO Abundances with BACCHUS

Much of the effort in this study involved deriving abundances for C, N, O, and the C isotopic ratio (^{12}C/^{13}C), which are all tracers of RSG nucleosynthesis and internal mixing. APOGEE derives abundances for these chemical elements (besides ^{12}C/^{13}C) through the ASPCAP pipeline. However, we seek to verify and improve these abundances by conducting our own spectral fitting analysis. Additionally, we seek to derive the ^{12}C/^{13}C abundance ratio by fitting relatively weak ^{13}C spectral features.

We employ the Brussels Automatic Code for Characterizing High accUracy Spectra (BACCHUS v84; Masseron et al. 2016) software to estimate abundances for C, O, N, Fe, Mg, Si, and ^{12}C/^{13}C in that order. For each star in our sample, stellar parameters such as T_{eff}, $\log g$, [M/H], [α/M],[5] microturbulent velocity, and macroturbulent velocity as determined by ASPCAP are input into BACCHUS to provide information to the program on how the star's observed spectrum should look based on these parameters.

BACCHUS operates by computing a variety of model spectra based on a grid of MARCS stellar atmosphere models (Gustafsson et al. 2008) and the 1D Local Thermodynamic Equilibrium Turbospectrum radiative transfer code (Alvarez & Plez 1998; Plez 2012). Each model spectrum represents a different abundance value[6] for the element that is being processed. For a given element, we provide a list of wavelengths for several spectral features in the H-band spectrum.

BACCHUS then goes through each spectral feature for each element and compares the observed and model spectra using several fitting methods. These fitting methods seek to find the best matching abundance value for each spectral feature. The abundances determined from each spectral feature for a given element are then averaged to provide a singular abundance value for that element. Figure 2 shows an example of what this fitting process looks like for one of the N spectral features.

[5]The abundance of α elements, such as O, Ne, Mg, Si, S, Ar, Ca, and Ti, compared to the total metallicity.

[6]BACCHUS computes abundances using the $\log \epsilon(X) = \log\left(\frac{N_X}{N_H}\right)$ format where N_X is the number of X atoms, and N_H is the number of H atoms.

The primary goal in this project is to determine C, N, O, and ^{12}C/^{13}C abundances. However, we also determine abundances for Fe, Mg, and Si because these elements are frequently found in the H-band spectra, and they can overlap, or blend with, the spectral features in which we are interested. Therefore, it is critical to gain an accurate representation of how influential these elements are by directly fitting for their abundances. These results help make realistic model spectra that include accurate, blending feature abundances. Furthermore, we iterate finding all abundances a total of three times to ensure that the fits and abundance results provided by BACCHUS are internally consistent.

While BACCHUS produces average abundance values for each element, it lacks by-eye verification of the quality of the fits. Using the BACCHUS fit results, we identified commonly well-fit spectral features, as well as spectral features that were poorly fit consistently for each element. We then recalculated average element abundances using only the consistently well-fit spectral features for a given element.

Additionally, we chose to adopt the abundances determined from the χ^2 minimization fitting method for almost all elements and spectral features. The exception to this choice is for the weak ^{13}C features in which the χ^2 method can often misrepresent the ^{13}C abundances. For measuring ^{13}C abundances, we utilized abundances estimated by the "wln" fitting method because it measures the abundance at the exact, input wavelength of the spectral feature. This precision ensures that we are measuring the ^{13}C spectral feature and not a feature nearby from a different element. We found that including these post-processing choices have noticeably improved the final C, N, O, and ^{12}C/^{13}C abundances.

Results

The preliminary results of this study are in Figures 3 and 4. A caveat that is relevant to Figure 3 is that the models overlaying the data are meant for a qualitative comparison to the observed trends rather than a strict, quantitative comparison. The reason for this statement is that the models presented here (from Georgy et al. 2013a) assume an initial mixture of heavy elements in the star similar to that found in the Sun. However, stars in the MCs are known to exhibit a different initial mixture of heavy elements (e.g., Kurt & Dufour 1998), which impacts the amount of that element seen in the star at later stages of evolution. Unfortunately, there is a lack of appropriate models in the literature to account for this detail, and there is lack of observational evidence to provide an initial LMC and SMC ^{13}C abundance. Therefore, one cannot scale the models to LMC- and SMC-appropriate metallicities easily for the purposes of Figure 3. It is, however, a reasonable assumption that the functional form of the models should be similar regardless of initial composition, which allows us to compare the given models to our data qualitatively.

Beginning with Figure 3, we show $\log(C/N)$ as a function of ^{12}C/^{13}C. During the RSG phase of evolution, the stars' convective envelopes mix intermediate CNO-cycle products like ^{14}N and ^{13}C to the surface from deep within the star. Therefore for extensive convective mixing, we expect $\log(C/N)$ and ^{12}C/^{13}C to be low in value as ^{14}N and ^{13}C increase at the expense of ^{12}C. It is also expected that initially rotating stars will experience more mixing and their $\log(C/N)$ and ^{12}C/^{13}C values will be lower than non-rotating stars. Several stars in our sample occupy this low-$\log(C/N)$, low-^{12}C/^{13}C region of the diagram, indicating that these stars have undergone extensive convective mixing and/or rotation to alter these abundances.

Furthermore, to investigate how these ratios change with stellar mass, the models suggest that more massive stars tend to have higher $\log(C/N)$ than less massive stars until the end of their evolution when the most massive stars have the lowest $\log(C/N)$. The group of massive LMC stars around $\log(C/N) \backsim 0.75$ could represent evidence

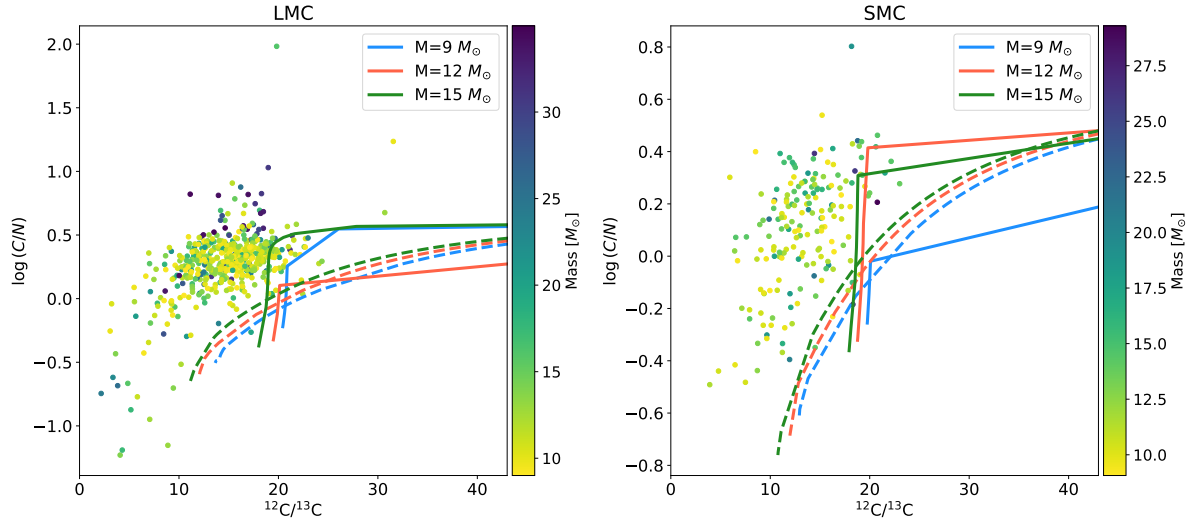

Figure 3: $\log C/N$ as a function of ^{12}C/^{13}C colored by stellar mass for the LMC (left) and SMC (right) RSGs. The models shown are from Georgy et al. (2013a) corresponding to LMC and SMC metallicities and for typical RSG masses. Solid-line models exhibit abundance predictions for no initial rotation, whereas dashed-line models represent stars with initial rotation rates equal to 30% of the critical rotation rate.

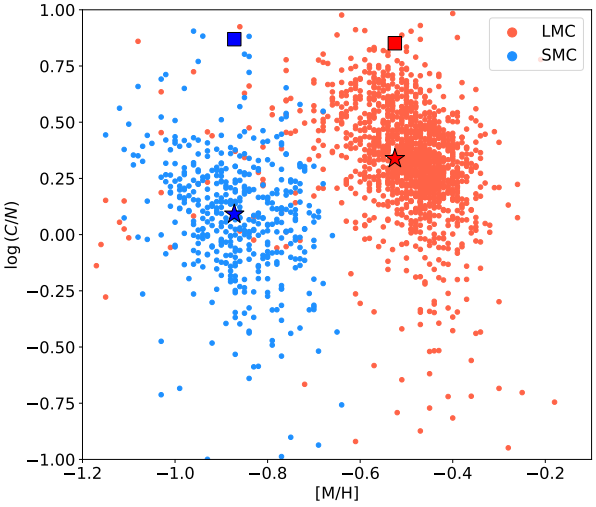

Figure 4: $\log(C/N)$ as a function of [M/H] (total stellar metallicity) for the LMC (red) and SMC (blue) RSGs. The square symbols represent the initial $\log(C/N)$ found in the LMC and SMC, whereas the star symbols show the average $\log(C/N)$ measured in the data.

of this intermediate-evolutionary phase where the more massive the star is, the higher its $\log(C/N)$ is. However, additional analysis and more accurate models are needed to definitively comment on this trend with stellar mass given that it is not as clear as to how the rest of the data are correlated with mass.

Next focusing on Figure 4, we show how $\log(C/N)$ varies with metallicity. Here, we wish to draw particular attention to comparing the LMC RSGs to the SMC RSGs as a whole by showing how the efficiency of mixing changes with metallicity. To address this point, we plot the estimated initial $\log(C/N)$ values in the LMC and SMC (Kurt & Dufour 1998) as square symbols, and we plot the observed, average $\log(C/N)$ for each sample as star symbols. We observe a larger difference between the initial and average $\log(C/N)$ values for the SMC ($\Delta\log(C/N) = -0.78$) compared to the LMC ($\Delta\log(C/N) = -0.51$). Also, the SMC produces a lower average $\log(C/N)$ than the LMC overall. These results suggest that mixing is more efficient at lower metallicities, as these low-metallicity RSGs bring a higher proportion of ^{14}N (with respect to ^{12}C) to their surfaces than higher metallicity RSGs.

Conclusions

In this work, we have isolated a sample of $\backsim$2,000 RSG stars in the nearby, low metallicity Magellanic Clouds. We estimated stellar parameters for these stars to better characterize them and to be able to compare them to theoretical models. Utilizing these stars' observed spectra from the APOGEE survey and the BACCHUS spectral analysis code, we derived C, N, O, and ^{12}C/^{13}C abundances. With these abundances, we sought to investigate current stellar evolution theory by gaining a greater understanding of how internal mixing occurring before and during the RSG phase of evolution affects stars' evolution and how mixing changes with stellar mass and metallicity.

Our initial results presented in Figure 3 provide evidence for RSG internal mixing in the form of low $\log(C/N)$ and ^{12}C/^{13}C. We also see that the most massive LMC RSGs exhibit relatively high $\log(C/N)$ for a given ^{12}C/^{13}C. These results suggest that either these stars have not yet undergone their full mixing episode to further reduce those ratios in accordance with the models, or there is perhaps a piece of physics that occurs in nature to alter these abundance ratios that is not accounted for in the models. Finally, Figure 4 supports the notion that internal mixing increases in efficiency as metallicity decreases.

One consequence of these results that may be affecting our data is that stars in low-metallicity environments may not proceed through the nominal evolutionary phases exactly as stellar evolution theory suggests. The inclusion of efficient internal mixing can significantly alter the source material available for stellar nucleosynthesis. Since nucleosynthesis determines global qualities of the star such as temperature, luminosity, and life time, stars with significantly modified composition gradients could evolve much more unusually than we expect.

Further analysis needs to be done to be able to quantitatively compare the theoretical model abundances with our observed abundances. Also, future effort will be focused on conducting a more robust estimate of stellar mass to be able to decipher any abundance correlations with stellar mass that exist. With these modifications, we will continue testing whether these stars experience altered conditions of stellar evolution, or if the effect of mixing is not as important to a star's evolution as it would initially seem.

Acknowledgements

CM would like to acknowledge the collaborators on this project and thank them for their support: Steven Majewski, Verne Smith, Christian Hayes, Katia Cunha, Thomas Masseron, Fábio Wanderley, and Maren Brauner.

Funding for the Sloan Digital Sky Survey IV has been provided by the Alfred P. Sloan Foundation, the U.S. Department of Energy Office of Science, and the Participating Institutions.

SDSS-IV acknowledges support and resources from the Center for High Performance Computing at the University of Utah. The SDSS website is www.sdss4.org.

SDSS-IV is managed by the Astrophysical Research Consortium for the Participating Institutions of the SDSS Collaboration including the Brazilian Participation Group, the Carnegie Institution for Science, Carnegie Mellon University, Center for Astrophysics — Harvard & Smithsonian, the Chilean Participation Group, the French Participation Group, Instituto de Astrofísica de Canarias, The Johns Hopkins University, Kavli Institute for the Physics and Mathematics of the Universe (IPMU) / University of Tokyo, the Korean Participation Group, Lawrence Berkeley National Laboratory, Leibniz Institut für Astrophysik Potsdam (AIP), Max-Planck-Institut für Astronomie (MPIA Heidelberg), Max-Planck-Institut für Astrophysik (MPA Garching), Max-Planck-Institut für Extraterrestrische Physik (MPE), National Astronomical Observatories of China, New Mexico State University, New York University, Uni-

versity of Notre Dame, Observatário Nacional / MCTI, The Ohio State University, Pennsylvania State University, Shanghai Astronomical Observatory, United Kingdom Participation Group, Universidad Nacional Autónoma de México, University of Arizona, University of Colorado Boulder, University of Oxford, University of Portsmouth, University of Utah, University of Virginia, University of Washington, University of Wisconsin, Vanderbilt University, and Yale University.

References

Abdurro'uf et al., 2022, ApJS, 259, 35

Allende Prieto C., Beers T. C., Wilhelm R., Newberg H. J., Rockosi C. M., Yanny B., Lee Y. S., 2006, ApJ, 636, 804

Alvarez R., Plez B., 1998, A&A, 330, 1109

Beaton R. L., et al., 2021, AJ, 162, 302

Blanton M. R., et al., 2017, AJ, 154, 28

Bowen I. S., Vaughan A. H. J., 1973, Appl. Opt., 12, 1430

Boyer M. L., et al., 2011, AJ, 142, 103

Cardelli J. A., Clayton G. C., Mathis J. S., 1989, ApJ, 345, 245

Cioni M. R. L., Girardi L., Marigo P., Habing H. J., 2006a, A&A, 448, 77

Cioni M. R. L., Girardi L., Marigo P., Habing H. J., 2006b, A&A, 452, 195

Davies B., Dessart L., 2019, MNRAS, 483, 887

Gaia Collaboration et al., 2021, A&A, 649, A7

García Pérez A. E., et al., 2016, AJ, 151, 144

Georgy C., Ekström S., Granada A., Meynet G., Mowlavi N., Eggenberger P., Maeder A., 2013a, A&A, 553, A24

Georgy C., et al., 2013b, A&A, 558, A103

Graczyk D., et al., 2020, ApJ, 904, 13

Gustafsson B., Edvardsson B., Eriksson K., Jørgensen U. G., Nordlund Å., Plez B., 2008, A&A, 486, 951

Hasselquist S., et al., 2021, ApJ, 923, 172

Jönsson H., et al., 2020, AJ, 160, 120

Kurt C. M., Dufour R. J., 1998, in Dufour R. J., Torres-Peimbert S., eds, Revista Mexicana de Astronomia y Astrofisica Conference Series Vol. 7, Revista Mexicana de Astronomia y Astrofisica Conference Series. p. 202

Kurucz R., 1993, Robert Kurucz CD-ROM, 13

Majewski S. R., et al., 2017, AJ, 154, 94

Mamajek E. E., et al., 2015, arXiv e-prints, p. arXiv:1510.06262

Masseron T., Merle T., Hawkins K., 2016, BACCHUS: Brussels Automatic Code for Characterizing High accUracy Spectra, Astrophysics Source Code Library, record ascl:1605.004 (ascl:1605.004)

Neugent K. F., Levesque E. M., Massey P., Morrell N. I., Drout M. R., 2020, ApJ, 900, 118

Nidever D. L., et al., 2015, AJ, 150, 173

Pietrzyński G., et al., 2019, Nature, 567, 200

Plez B., 2012, Turbospectrum: Code for spectral synthesis, Astrophysics Source Code Library, record ascl:1205.004

Santana F. A., et al., 2021, AJ, 162, 303

Skrutskie M. F., et al., 2006, AJ, 131, 1163

Smith V. V., et al., 2021, AJ, 161, 254

Wilson J. C., et al., 2019, PASP, 131, 055001

Zasowski G., et al., 2017, AJ, 154, 198